THE ASTROPHYSICAL JOURNAL, 554:161–172, 2001 June 10

X-RAY OBSERVATIONS OF THE NEW PULSAR–SUPERNOVA REMNANT SYSTEM PSR J1119−6127 AND SUPERNOVA REMNANT G292.2−0.5

M. J. PIVOVAROFF,[1,2] V. M. KASPI,[1,3,4] F. CAMILO,[5] B. M. GAENSLER,[1,6] AND F. CRAWFORD[1,7]

Received 2000 September 18; accepted 2001 February 9

ABSTRACT

PSR J1119−6127 is a recently discovered 1600-yr-old radio pulsar that has a very high inferred surface dipolar magnetic field. We present a detailed analysis of a pointed *ASCA* observation and archival *ROSAT* data of PSR J1119−6127 and its surroundings. Both data sets reveal extended emission coincident with the newly discovered radio supernova remnant G292.2−0.5, which is reported in a companion paper by Crawford et al. A hard point source, offset ∼1′.5 from the position of the radio pulsar, is seen with the *ASCA* Gas Imaging Spectrometer (GIS). No pulsations are detected at the radio period with a pulsed fraction upper limit of 61% (95% confidence). The limited statistics prevent a detailed spectral analysis, although a power-law model with photon index $\Gamma \approx 1$–2 describes the data well. Both the spectral model and derived X-ray luminosity are consistent with those measured for other young radio pulsars, although the spatial offset renders an identification of the source as the X-ray counterpart of the pulsar uncertain.

Subject headings: ISM: individual (G292.2−0.5, AX J1119.1−6128.5) — pulsars: individual (J1119−6127) — stars: neutron — supernova remnants — X-rays: stars

1. INTRODUCTION

X-ray observations of young rotation-powered pulsars offer a unique opportunity to resolve several fundamental questions about neutron stars and supernova remnants. Studying the spectrum and morphology of the pulsar's synchrotron nebula (or plerion; Weiler & Panagia 1978) is crucial for determining basic properties about the relativistic pulsar wind and probing the density of the surrounding medium. Measuring the temperature of the cooling surface of the pulsar provides a way to understand the thermal evolution of neutron stars and to constrain the equation of state. Additionally, X-ray observations of pulsars are also important for searching for the remnant of the supernova that created the pulsar. Direct studies of the remnant are useful for numerous reasons, including measurement of the elemental abundances and determination of the shock conditions in the supernova remnant (SNR) through spectral analysis. Associations between pulsars and SNRs can provide independent distance and age estimates for both objects and, with a statistically significant sample of associations, constraints on the birth properties of neutron stars, including initial period, magnetic field, and velocity distribution, can be found.

PSR J1119−6127 was discovered by Camilo et al. (2000) in an ongoing survey for pulsars in the Galactic plane using the Parkes 64 m radio telescope in Australia. Its spin period of $P = 0.4$ s is long compared with those of young Crab-like pulsars, but its period derivative of $\dot{P} = 4 \times 10^{-12}$ is extremely large. The characteristic age calculated from these parameters is only $\tau_c \equiv P/2\dot{P} = 1600$ yr. In addition to its extreme youth, PSR J1119−6127 also has a very large inferred surface dipole magnetic field strength, $B \simeq 3.2 \times 10^{19}(P\dot{P})^{1/2}\ \mathrm{G} = 4 \times 10^{13}\ \mathrm{G}$.

PSR J1119−6127 is also noteworthy as it is one of only five pulsars that has an accurately measured second period derivative, $\ddot{P}$, which allows determination of the braking index. In many ways, PSR J1119−6127 is similar to PSR B1509−58, another long-period young pulsar for which the braking index is measured. Table 1 presents the spin parameters and derived quantities for both of these pulsars. In the same way that PSR B0540−69 and the Crab pulsar establish the existence of a class of rapidly spinning young pulsars with large spin-down luminosities, PSR J1119−6127 and PSR B1509−58 suggest the existence of a class of equally young pulsars but with higher magnetic fields, longer periods, and much lower spin-down luminosities.

After the pulsar's discovery, relevant publicly accessible data archives were searched for observations with PSR J1119−6127 in their field of view. A survey of the Galaxy performed with the Molonglo Observatory Synthesis Telescope (MOST) at 843 MHz (Green et al. 1999) revealed a faint ringlike shell, ∼15′ in extent and approximately centered on the position of the pulsar. A brief *ROSAT* PSPC observation shows X-ray emission coincident with a portion of the radio shell. Recently, radio interferometric observations of PSR J1119−6127 and its vicinity have been made with the Australia Telescope Compact Array (ATCA) (Crawford 2000; Crawford et al. 2001). The radio data confirm the existence of the shell-like emission and show that it has the nonthermal spectrum characteristic of a shell SNR. This paper presents a detailed analysis of both a pointed *ASCA* and the serendipitous *ROSAT* observation.

[1] Department of Physics and Center for Space Research, Massachusetts Institute of Technology, Cambridge, MA 02139; mjp@space.mit.edu, bmg@space.mit.edu.

[2] Current address: Therma-Wave, Inc., 1250 Reliance Way, Fremont, CA 94539.

[3] Department of Physics, Rutherford Physics Building, McGill University, 3600 University Street, Montreal, QC H3A 2T8, Canada; vkaspi@physics.mcgill.ca.

[4] Alfred P. Sloan Research Fellow.

[5] Columbia Astrophysics Laboratory, Columbia University, 550 West 120th Street, New York, NY 10027; fernando@astro.columbia.edu.

[6] Hubble Fellow.

[7] Current address: Management and Data Systems Division, Lockheed Martin Corporation, P.O. Box 8048, Philadelphia, PA 19101; crawford@space.mit.edu.

TABLE 1

ASTROMETRIC AND SPIN PARAMETERS FOR PSRs J1119−6127 AND B1509−58

Parameter	PSR J1119−6127	PSR B1509−58
Right ascension (J2000)	11 19 14.30	15 13 55.62
Declination (J2000)	−61 27 48.5	−59 08 09.0
Period, P (ms)	407.64	150.66
Period derivative, $\dot{P}$	4.023×10^{-12}	1.537×10^{-12}
Second period derivative, $\ddot{P}$	3.59×10^{-23}	1.31×10^{-23}
Epoch of period (MJD)	51173.0	48355.0
Braking index	2.91 ± 0.05	2.837 ± 0.001
Dispersion measure, DM (pc cm^{-3})	707	253
Characteristic age, τ_c (yr)	1606	1554
Spin-down luminosity, $\dot{E}$ (ergs s^{-1})	2.3×10^{36}	1.8×10^{37}
Magnetic dipole field strength, B (G)	4.1×10^{13}	1.5×10^{13}
Reference	Camilo et al. 2000	Kaspi et al. 1994

NOTE.—Units of right ascension are hours, minutes, and seconds, and units of declination are degrees, arcminutes, and arcseconds.

2. OBSERVATIONS

The *ASCA* X-ray telescope (Tanaka, Inoue, & Holt 1994) was used to observe PSR J1119−6127 during a 36 hr period spanning 1999 August 14–15 as part of the AO-7 Guest Observer program (sequence number 57040000). To achieve the time resolution necessary for pulsation searches, the GIS (Gas Imaging Spectrometer) was operated in a nonstandard mode. A time resolution of 0.488 or 3.91 ms (depending on the telemetry rate) was achieved by sacrificing information about the time characteristics (or "Risetime") of detected events, which is one way to differentiate between background and celestial X-ray photons (see §§ 3.1.1 and 3.2 for a discussion of other ramifications of this operation mode).

As a compromise between having a field of view (FOV) wide enough to encompass a large fraction of the shell and obtaining potentially useful spectroscopic information from the CCDs, the SIS (Solid-State Imaging Spectrometer) was operated in two-chip mode, providing an imaging area $22' \times 11'$. The data were analyzed using the standard (i.e., REV 2) screening criteria suggested in *The ASCA Data Reduction Guide*.[8] The resulting effective exposure times are 37 ks (GIS) and 34 ks (SIS).

The *ROSAT* X-ray telescope (Trümper 1982) serendipitously observed the field around PSR J1119−6127 with the Position Sensitive Proportional Counter (PSPC) on 1996 August 14 during an 11 ks pointed observation of NGC 3603 (sequence number RP900526N00). After retrieving the data from the NASA-maintained HEASARC archive, we used the already processed and filtered data for our subsequent analysis. In the observation, PSR J1119−6127 is located 31′ away from the optical axis, and because of vignetting and obscuration from the mirror support structure, the effective exposure time for a 15′ diameter circle centered on the pulsar is between 6.4 and 8.9 ks.

3. DATA REDUCTION

3.1. *Image Analysis*

3.1.1. *ASCA*

Flat-fielded images were generated by aligning and coadding exposure-corrected images from pairs of instruments. As discussed by Pivovaroff, Kaspi, & Gotthelf (2000b), great care must be taken (particularly for the GIS) to remove detector artifacts (e.g., the window support grid) and the diffuse X-ray background (XRB). The software employed includes the recently released FTOOL "mkgisbgd."[9] For a complete discussion of the steps taken to make this software compatible with this observation, see chapter 7 of Pivovaroff (2000).[10]

After rebinning the SIS data by a factor of 4 (6.″73 pixel^{-1}), data from both instruments were smoothed with a kernel representing the point-spread function (PSF) of the X-ray telescope (XRT) and detector combination. We approximate this function with a Gaussian of $\sigma = 30''$ for the SIS and $\sigma = 45''$ for the GIS. Finally, we correct the astrometric position of the smoothed images for known errors in the pointing solution using the FTOOL "offsetcoord."[11]

X-ray events were filtered by energy to make images in three different bands: soft (0.8–3.0 keV), hard (3.0–10.0 keV), and broad (0.8–10.0 keV). Figure 1 shows GIS images for all three bands (soft [*top left*], hard [*bottom left*], and broad [*top right*]). Given the similarities between the two instruments, only the hardband SIS image is shown (*bottom right*). In each plot, the radio position of PSR J1119−6127 is marked by a cross. Each plot also displays the contours from the recent 1.4 GHz ATCA radio observations of the field around the pulsar (Crawford et al. 2001). Both instruments show significant emission from a nearly circular region that roughly matches the radio SNR morphology. On the basis of this and other evidence presented below, we classify this extended emission as the previously unidentified X-ray–bright supernova remnant G292.2−0.5. The right (western) side of the SNR exhibits marked enhancements in X-ray flux at energies below 3 keV, while at higher energies the emission is relatively uniform throughout the SNR.

In addition to the X-ray–bright SNR, the GIS shows evidence for a hard pointlike source in the middle of G292.2−0.5. Following the procedure of Pivovaroff, Kaspi, & Camilo (2000a), we estimate the significance of this detec-

[8] See http://legacy.gsfc.nasa.gov/docs/asca/abc/abc.html.

[9] See http://heasarc.gsfc.nasa.gov/docs/asca/mkgisbgd/mkgisbgd.html.

[10] An on-line version of this text may be found at http://space.mit.edu/ACIS/mjp_publications/thesis.html.

[11] Refer to http://heasarc.gsfc.nasa.gov/docs/asca/coord/updatecoord.html for details.

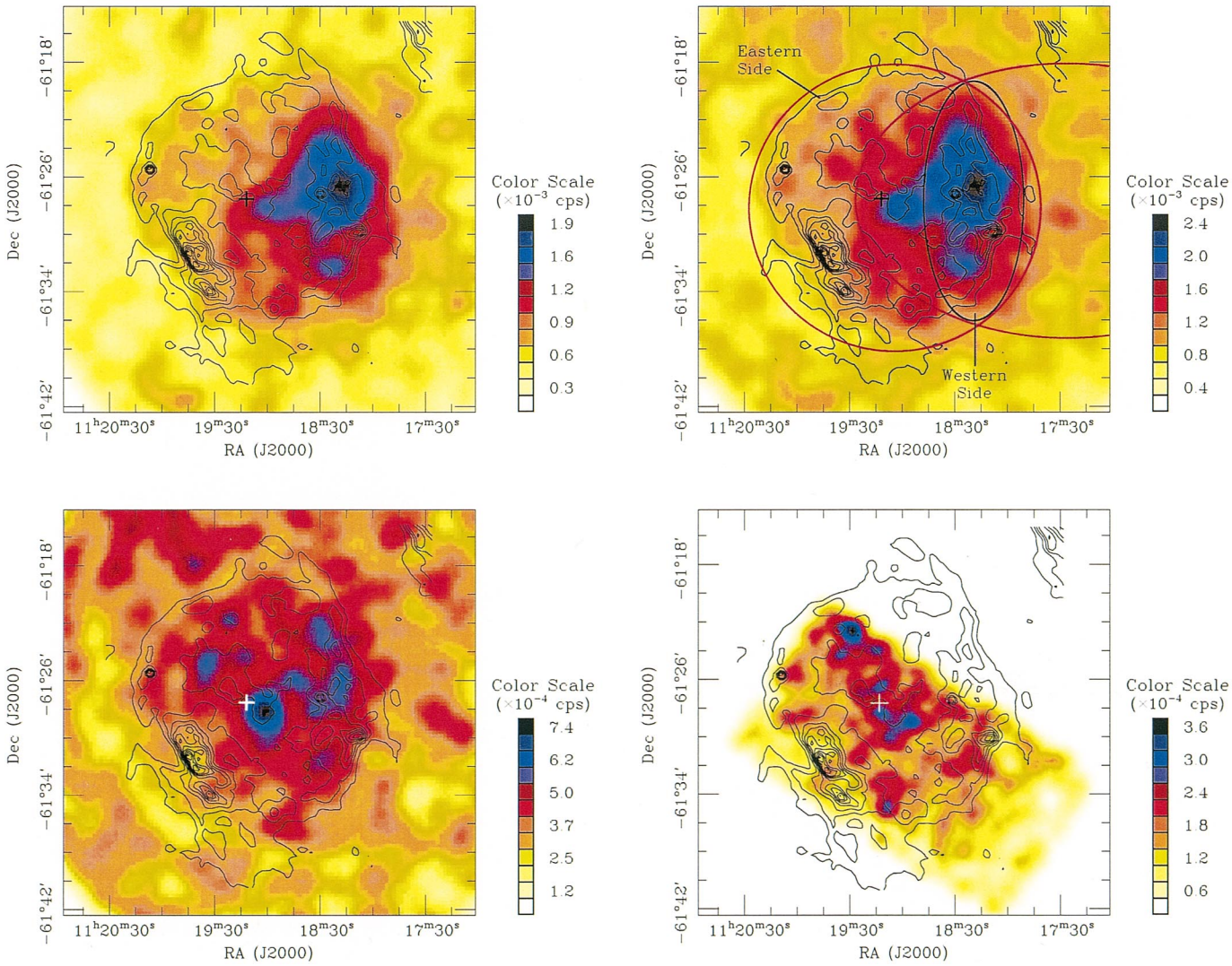

FIG. 1.—*ASCA* images of the field around PSR J1119−6127. Images are made in three separate energy bands: softband (0.8–3.0 keV), hardband (3.0–10.0 keV), and broadband (0.8–10.0 keV). GIS images are shown for each band: soft (*top left*), hard (*bottom left*), and broad (*top right*). For comparison, the SIS hardband image is also shown (*bottom right*). In each image, the location of PSR J1119−6127 is marked by a cross. Contours are from 1.4 GHz ATCA observations and range from 5% to 95% of the maximum value (39 mJy beam^{-1}) in increments of 15% (Crawford et al. 2001). Color bars in each plot indicate counts s^{-1} arcmin^{-2}. The X-ray emission, classified here as the previously unknown SNR G292.2−0.5, roughly traces the radio morphology in the broad and soft bands, although significant enhancement is seen on the western (*right*) side of the SNR below 3 keV. A hard pointlike source is clearly evident in the GIS image. The GIS broadband image also shows the two regions used to extract spectra of the SNR.

tion by comparing the number of photons detected in a small aperture centered on the source with those from a concentric annulus used to estimate the local background. We calculate a significance of $\sigma \gtrsim 4.0$ for the 158 background-subtracted photons detected with energies between 3.0 and 10.0 keV. To explore the possibility that the source is an instrumental artifact, we examined individual images from GIS-2 and GIS-3. Emission is present in both detectors at the above position, verifying the celestial nature of the source.

No pointlike source is seen in the hardband SIS image, although there is enhanced emission at the source position derived from the GIS data. Using aperture and annulus radii (2.′0, 3.′25, and 4.′5, respectively) appropriate for the smaller SIS+XRT PSF, we calculate a significance of $\sigma \gtrsim 3.5$ for the 59 background-subtracted photons detected between 3.0 and 10.0 keV. The lack of a more significant pointlike feature in the SIS when one is present in the GIS is not uncommon and probably results from the larger effective area of the GIS at high energies (E. V. Gotthelf 2000, private communication).

Fitting a two-dimensional Gaussian to the GIS source distribution, we measure a position (J2000) of R.A. = $11^{h}19^{m}03^{s}.4$, decl. = $-61°28'30''$ with an uncertainty of $\sim 10''$. We classify this source as AX J1119.1−6128.5. The absolute pointing uncertainty of the GIS, after making the known corrections mentioned above, has an error radius of 24″ at the 90% confidence level (Gotthelf et al. 2000a). The source is located 87″ away from PSR J1119−6127, more than twice the combined positional errors. However, we note that in at least one documented case, the *ASCA*-measured position of a source was 80″ from the well-established position (Gotthelf et al. 2000a). Thus, while the offset of the GIS source from the pulsar is larger than expected, it does

not preclude the possibility that the source is the X-ray counterpart of PSR J1119−6127, especially if other evidence supports the association.

3.1.2. *ROSAT*

Using standard software available from HEASARC, we produced flat-fielded images with 15′ pixels in the standard *ROSAT* soft (0.1−0.4 keV) and hard (0.5−2.0 keV) bands. The flat-fielded images were then smoothed with a Gaussian kernel ($\sigma = 1\farcm25$) to approximate the PSF of the telescope at the off-axis position of the pulsar. Figure 2 shows the resultant images for the soft (*left*) and hard (*right*) bands. A cross marks the position of PSR J1119−6127 and the contours are from the ATCA observations (Crawford et al. 2001). No emission from the SNR is detected in the soft band. However, in the hard band, emission coincident with the western side of the radio shell is strongly detected. No X-rays are detected from the pulsar in either band. The morphology of the hard *ROSAT* band (0.5–2.0 keV; Fig. 2 [*right*]) agrees well with that of the soft GIS band (0.8–3.0 keV; Fig. 1 [*top left*]).

The agreement between the two telescopes offers, in principle, the chance to check the absolute pointing of *ASCA*. Because of its large FOV (2° diameter) and its soft-energy sensitivity, the PSPC usually detects emission from several nearby stars in any given pointing. The positions of well-resolved point sources were checked for optical counterparts using the SIMBAD catalog.[12] Four bright stars were found, and the mean offset between the optical and X-ray positions was 18″. Thus, we take the absolute position uncertainty of these PSPC data to be 18″. Next, we cross-correlated the morphology between the PSPC and GIS data. Unfortunately, the approximate arcminute spatial resolution of both images, combined with the different responses of both instruments, makes a detailed alignment check impossible. While an offset of more than ∼1′ between the *ASCA* and *ROSAT* observations can be ruled out, this does not represent an improvement on the *ASCA* positional uncertainty of 0.′5 already discussed.

[12] See http://cdsweb.u-strasbg.fr/Simbad.html.

3.2. *Timing Analysis*

Pulsations from PSR J1119−6127 were searched for by extracting GIS events from a circular region centered on the position of AX J1119.1−6128.5. After the arrival times were reduced to the barycenter using the FTOOL "timeconv," the data were folded using 10 phase bins using the radio ephemeris corresponding to the mean MJD of the *ASCA* observation. Although the *ASCA* observation of PSR J1119−6127 occurred very close to the time the pulsar glitched (Camilo et al. 2000), given the small differences in the pre- and post-glitch values of P and $\dot{P}$ and the total time span of our observation, the glitch is irrelevant to our analysis.

The emission from G292.2−0.5 significantly contaminates the signal from AX J1119.1−6128.5 and could prevent the detection of X-ray pulsations from PSR J1119−6127. To minimize this possibility, we extracted data using combinations of four different aperture radii (ranging between 2′ and 5′ in increments of 1′) and twelve different energy bands (e.g., 0.8–10.0 keV and 1.0–5.0 keV). All resultant pulse profiles were searched for pulsations using both the H-test (de Jager 1994) and χ^2 (Leahy et al. 1983). No pulsations were found in any data set.

Using the method of Brazier (1994), we find a 95% confidence upper limit on the pulsed flux of 61% for data in the energy range 3.0–10.0 keV within a 3′ radius of AX J1119.1−6128.5. The upper limit is not particularly constraining, in part because of our use of the nonstandard observing mode which made pulsation searching possible. As discussed in § 2, sacrificing Risetime information limits *ASCA*'s ability to differentiate between Earth-orbit–related background and celestial X-rays. In particular, 2 hr binning of time series extracted from different locations in the GIS field of view reveals common trends (specifically, a rise and decline in the count rate by a factor of ∼3 over a ∼6 hr period) that cannot be celestial. Such behavior does not

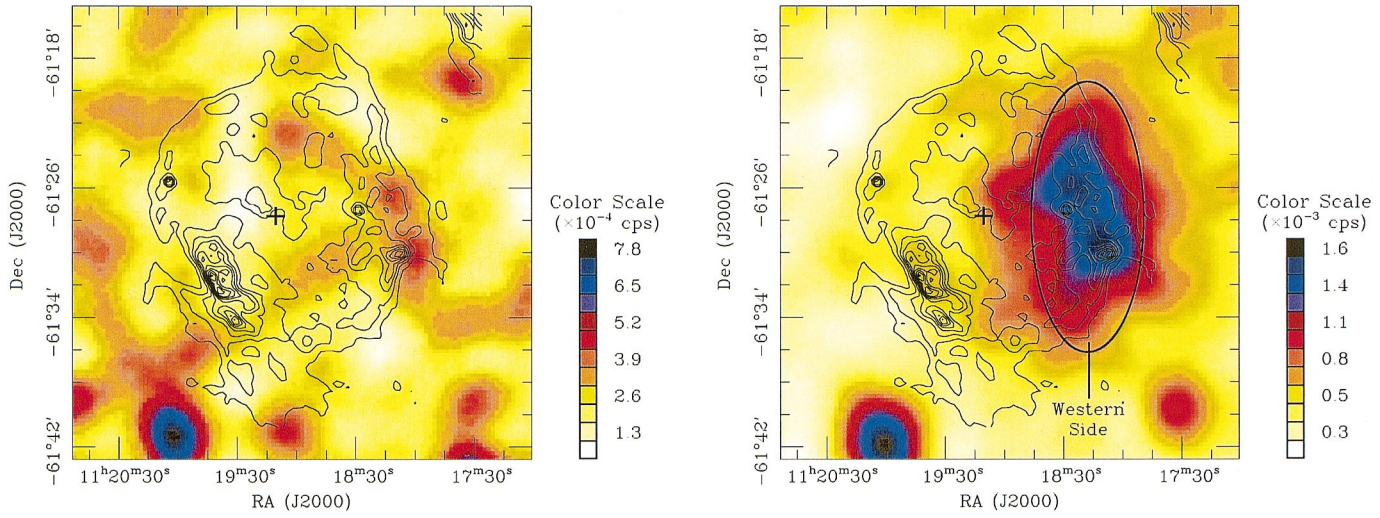

FIG. 2.—*ROSAT* PSPC images of the field around PSR J1119−6127. In each image, the location of PSR J1119−6127 is marked by a cross. Contours are from 1.4 GHZ ATCA radio observations, as in Fig. 1. Color bars in each plot indicate counts s^{-1} $arcmin^{-2}$. *Left:* The softband (0.1–0.4 keV) image shows no emission coincident with either the radio contours or the pulsar. *Right:* The hard-band (0.5–2.0 keV) image clearly shows emission from the western side of the SNR and has the same morphology and intensity distribution as the softband GIS image (Fig. 1 [*top left*]). The heavy ellipse marks the region used to extract a spectrum from the SNR. No X-ray counterpart to PSR J1119−6127 is visible in either band.

significantly affect our spectral analysis or the observed morphology of emission, however.

3.3. *Spectral Analysis*

We restricted our spectral work to only the *ASCA* GIS and *ROSAT* PSPC data.[13] We defined regions where it is appropriate to sum counts together and construct a single spectrum for a given area. One such region is the western side of the SNR, bright in soft X-rays. We extracted a spectrum for both the GIS and PSPC from an ellipse $17' \times 7'$ in extent, with major axis parallel to lines of constant right ascension and centered in the middle of the bright SNR emission. A natural complement to this spectrum is one drawn from the eastern side of G292.2−0.5. Here, only the GIS, with its high-energy (i.e., $E > 2$ keV) sensitivity, can provide spectroscopic information. In this case, the spectrum is drawn from a crescent-shaped region that is slightly larger than the radio shell and excludes the point source and the western side. These regions are shown in Figures 1 (*top right*) and 2 (*right*). We also extracted a GIS spectrum for the point source from a circular region with radius of 2.5. The data from GIS-2 and GIS-3 were kept separate to avoid complications associated with summing them into a single spectrum.

3.3.1. *G292.2−0.5*

The PSFs of both *ASCA* and *ROSAT* result in a contamination of the source flux with diffuse XRB. A background spectrum must therefore be subtracted from the data. Ideally, the background should be taken from a nearby region that is source free and located at the same off-axis angle, which not only accounts for the XRB but for any local diffuse emission, always a possibility when looking in the Galactic plane. While this task is trivial for the PSPC and its 2° FOV, the situation is more difficult for the GIS. With more than 50% of the GIS FOV unoccupied by G292.2−0.5, it might appear this region is appropriate for extracting a background. However, the scattering properties and broad wings of the XRT result in reflection properties that are strongly dependent on both incident energy and off-axis angle (see, e.g., Gendreau 1995). Instead, we use another feature of the "mkgisbgd" FTOOL to construct an accurate background. We again refer the interested reader to Pivovaroff (2000).

[13] Because of the continual radiation damage suffered by the CCDs, spectral data from the SIS this late in *ASCA*'s life is highly suspect (see, e.g., Ueda et al. 1999).

Our initial attempts at spectral fitting indicated that all five data sets could be described by a single model, as long as we allowed for different normalization values for each telescope and unique column densities ($N_{\rm H}$) for each side of the SNR. In total, there were six free parameters: two values of $N_{\rm H}$, the spectral characterization (e.g., temperature for a plasma model), and three normalization values, two for the western side (GIS-2+GIS-3 and PSPC) and one for the eastern side (GIS-2+GIS-3). The energy range fit is restricted to those bands where the signal is statistically significant: 0.4–2.0 keV (PSPC), 0.7–7.0 keV (GIS—western side), 0.7–8.0 keV (GIS—eastern side). Data were then rebinned such that each background-subtracted energy bin had a minimum of 20 counts, allowing us to use the χ^2 statistic as our goodness-of-fit estimator. All fitting was performed with XSPEC v.10.0 using standard models.

We use a thermal bremsstrahlung model and the MEKAL[14] plasma model as representative thermal spectra and a simple power law to explore nonthermal models. Elemental abundances have been frozen at the values determined by Anders & Grevesse (1989). Table 2 lists the results of our fits, including derived parameters and their 90% confidence limits. The measured absorbed fluxes for the western region are $F_{0.7-7.0\,\rm keV} = 2 \times 10^{-12}$ ergs s^{-1} cm^{-2} (*ASCA*) and $F_{0.4-2.0\,\rm keV} = 7 \times 10^{-13}$ ergs s^{-1} cm^{-2} (*ROSAT*); for the eastern region, it is $F_{0.7-8.0\,\rm keV} = 3 \times 10^{-12}$ ergs s^{-1} cm^{-2} (*ASCA*). Although the power-law model has the lowest χ^2, the *F*-test (see, e.g., Bevington & Robinson 1992) indicates that all three models describe the data equally well. The rather large reduced χ^2 values ($\chi^2_\nu = 1.6$–1.7) indicate a systematic discrepancy between the data and each model.

Figure 3 displays spectra from different regions of G292.2−0.5. For clarity, we present the data for a given region and instrument separately: PSPC western side (*top*), GIS western side (*middle*), GIS eastern side (*bottom*). Each panel also plots the best-fit power-law model. (We note that because of the moderate spectral resolution of both the GIS and PSPC, the thermal models have a similar shape to the nonthermal one shown.) The large χ^2 is mainly attributable to systematic error, easily seen in the residuals below 2 keV in the spectra from the western side and above 5 keV in the spectra from the eastern side. Attempts to improve the fit by addition of a second spectral component do not work for two reasons. First, while some of the excess residuals appear

[14] See http://heasarc.gsfc.nasa.gov/docs/journal/meka6.html.

TABLE 2

SPECTRAL FIT PARAMETERS FOR SNR G292.2−0.5

			Western Side			Eastern Side		
Model	kT (keV)	Photon Index	$N_{\rm H}$ (10^{22} cm^{-2})	Norm[a] (10^{-3})	Norm[b] (10^{-3})	$N_{\rm H}$ (10^{22} cm^{-2})	Norm[a] (10^{-3})	χ^2/dof
Power-law.....	...	2.3 ± 0.1	$0.28^{+0.07}_{-0.06}$	$0.97^{+0.13}_{-0.11}$	$0.62^{+0.12}_{-0.11}$	1.6 ± 0.2	$2.0^{+0.4}_{-0.3}$	332/211
T.B.	$4.1^{+0.6}_{-0.5}$	...	$0.11^{+0.05}_{-0.04}$	$0.81^{+0.07}_{-0.06}$	$0.51^{+0.09}_{-0.08}$	1.3 ± 0.2	1.6 ± 0.2	366/211
MEKAL	$3.5^{+0.4}_{-0.3}$	...	$0.16^{+0.06}_{-0.05}$	2.0 ± 0.1	1.3 ± 0.2	1.5 ± 0.2	4.2 ± 0.4	351/211

NOTE.—T.B. refers to thermal bremsstrahlung. Norm refers to the normalization used for a particular model: power law—(photons keV^{-1} cm^{-2} s^{-1}), thermal bremsstrahlung—$([3.02 \times 10^{-15}/(4\pi D^2)] \int n_e n_I \, dV)$, where n_e and n_I are the local electron and ion densities and D is the distance, or MEKAL—$([10^{-15}/(4\pi D^2)] \int n_e n_H \, dV)$, where $n_{\rm H}$ is the local hydrogen density. All uncertainties represent the 90% confidence limits.

[a] Parameter for the *ASCA* (GIS-2+GIS-3) data.

[b] Parameter for the *ROSAT* PSPC data.

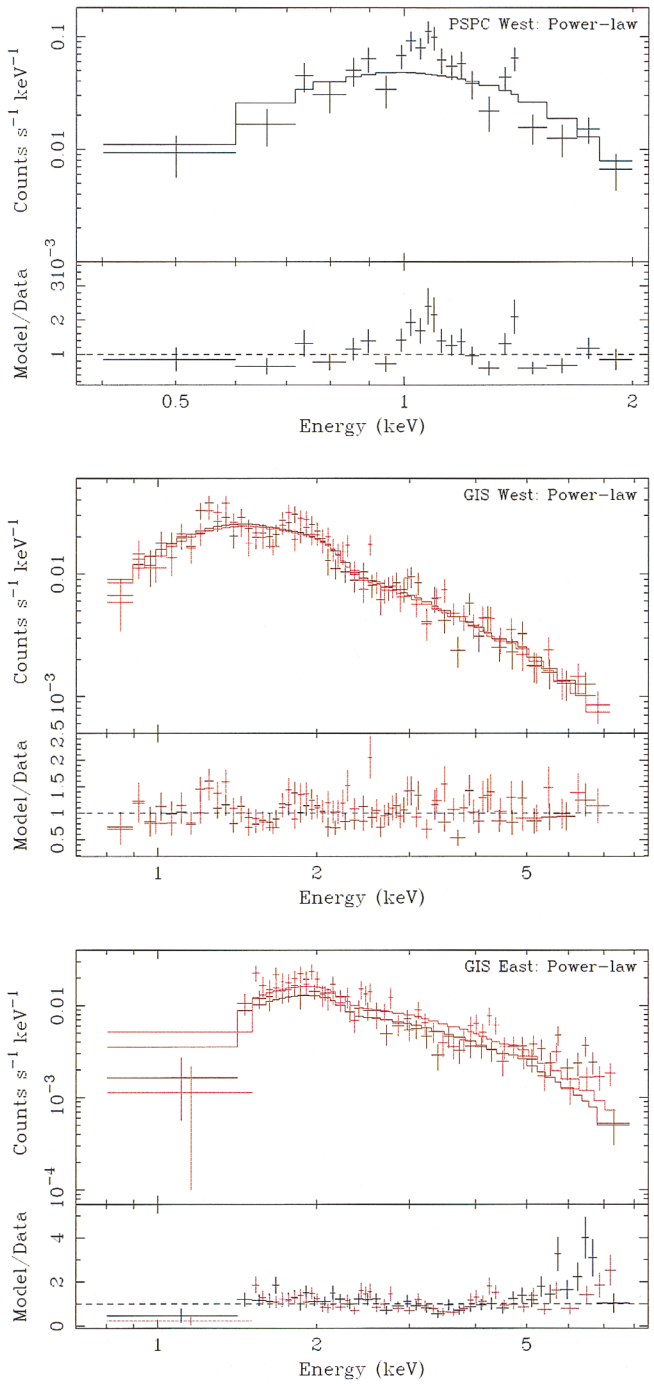

FIG. 3.—*ASCA* GIS and *ROSAT* PSPC spectra of G292.2−0.5. The PSPC (*top*) and GIS (*middle*) spectra from the western side of the SNR are very soft compared with the highly absorbed GIS spectrum (*bottom*) of the eastern side. Solid lines represent the best-fit power-law model to the data. In the bottom two panels, data from GIS-2 are in black and data from GIS-3 in red.

to be emission-like features, there are no known lines at these energies. Second, although the approximately 1000 counts in each GIS spectrum and the 500 counts in the PSPC spectrum allow a fairly tight constraint on a single model, there is not sufficient data to fit a combination of two models.

3.3.2. *AX J1119.1−6128.5*

Since the number of point-source photons was low (173 background-subtracted counts between 0.7 and 5.0 keV), fitting a spectrum is difficult. Given that it is not detected with *ROSAT* or in the soft band of the GIS, this source must either be intrinsically hard (e.g., temperature of several to tens of keV) or highly absorbed. With three times more events in the 2.0–5.0 keV band than in the 0.7–2.0 keV band and very few events above 5 keV, either scenario is plausible.

Because of the limited statistics, it is impossible to fit the spectrum when all three parameters ($N_{\rm H}$, kT or Γ, and normalization) are allowed to vary. Instead, we only required 10 background-subtracted counts per energy bin and fixed the column density at $N_{\rm H} = 1.5 \times 10^{22}$ cm^{-2}, the value determined using the MEKAL model for the eastern side of G292.2−0.5. While these modifications to the fitting scheme, compared with those used for G292.2−0.5, introduce additional uncertainty, they do allow at least a coarse characterization of the spectral nature of the point source.

For a power-law model, the photon index is $\Gamma = 1.4^{+1.0}_{-1.2}$ and the normalization is $(8 \pm 8) \times 10^{-5}$. For a thermal bremsstrahlung model, the temperature is $kT = 13^{+\infty}_{-11}$ keV and the normalization is $(1^{+0.9}_{-0.3}) \times 10^{-5}$. (Here, the upper limit on kT reflects the lack of *ASCA*'s response above 10 keV. Refer to Table 2 for the normalization units.) The measured absorbed flux is $F_{0.7-5.0\rm keV} = 2 \times 10^{-13}$ ergs s^{-1} cm^{-2}.

4. DISCUSSION

4.1. *General Properties of G292.2−0.5*

One of the main arguments supporting the interpretation of the extended X-ray emission as an SNR is its correlation with the morphology of the radio shell, recently shown to have radio spectral properties consistent with those of other known SNRs (Crawford et al. 2001). The presence of PSR J1119−6127 at the center of the radio and X-ray emission strengthens this reasoning and provides a way to test the consistency of the claimed association. If PSR J1119−6127 and G292.2−0.5 are the end products of the same supernova, their ages should be the same and the properties of the SNR should be those of a young remnant.

The age of PSR J1119−6127 as estimated from its spin parameters is 1700 ± 100 yr (Camilo et al. 2000). This assumes that the initial spin period P_0 of the neutron star was very small compared with that of the present one; if, however, P_0 were larger, the age would be smaller. In any case, as measured from the spin parameters, ∼1800 yr represents a good upper limit on the age, as the braking index has been measured (Table 1).

A distance estimate can be obtained from the Taylor & Cordes (1993) DM-distance relationship. The DM of PSR J1119−6127 implies a distance of more than 30 kpc, well outside the Galaxy. This implausibly large value is easily understood, as the Galactic longitude of PSR J1119−6127 ($l = 292°$) is nearly tangential to the Carina spiral arm, intersecting it at distances of 2.4 and 8.0 kpc. The best explanation for the large DM is that there is clumping of dense, dispersive material in the direction of the pulsar. The Taylor & Cordes model, which lacks fine structure (i.e., small-scale clumps), likely underestimates the electron density and, hence, overestimates the distance for this line of sight. A reasonable upper limit on the distance can be obtained by assuming that PSR J1119−6127 lies no farther than the second intersection point, or 8 kpc. We also note that in this direction, the edge of the Galaxy only extends

$\sim$10 kpc from the Sun (Georgelin & Georgelin 1976; Taylor & Cordes 1993), resulting in a maximum error on the distance upper limit of 25%. We adopt a compromise distance of 5 kpc for the calculations below.

The diameter of G292.2−0.5 extends $\sim 15'$ in radio and $\sim 17'$ in X-rays. The slightly larger extent in X-rays may be real or an artifact of the larger PSFs of *ASCA* and *ROSAT* as compared to the ATCA beam size. We adopt an angular size of $(15 \pm 2)'$ to encompass both measurements. Taken with the age and distance estimates, we calculate a mean expansion velocity of $v = (6.2 \pm 0.9)D_5 \times 10^3$ km s^{-1}, where D_5 is the distance to the pulsar parameterized in units of 5 kpc. This velocity is consistent with that of a 1700-yr-old SNR still evolving in the free expansion phase. It implies a kinetic energy for the initial explosion of $E_{51} = (0.4 \pm 0.1)M_{\rm ej}\ D_5^2$, where E_{51} is the explosion energy in units of 10^{51} ergs and $M_{\rm ej}$ is the ejected mass in solar masses.

G292.2−0.5 may also be in the Sedov-Taylor (ST) phase. For adiabatic expansion, $r_{\rm SNR} = 1.15(Et^2/\rho)^{1/5}$ (Taylor 1950; Sedov 1959), where $r_{\rm SNR}$ is the linear radius of the SNR, E is the explosion energy, t is the SNR's age, and ρ is the mass density of the ambient medium into which the SNR is expanding. Using the measured size of the SNR and recasting in terms of the ambient particle density n, $E_{51}/n = (12 \pm 8)D_5^5$. Remnants only enter ST evolution after sweeping up $\sim 20M_{\rm ej}$ (Fabian, Brinkmann, & Stewart 1983; Dohm-Palmer & Jones 1996). We estimate the material swept up by the SNR by assuming a constant density $\rho = nm_{\rm H}$ inside the volume occupied by G292.2−0.5; this requires $n > (0.16 \pm 0.08)M_{\rm ej}\ D_5^{-3}$ cm^{-3}. Therefore, $E_{51} > (2.0 \pm 1.6)M_{\rm ej}D_5^2$.

Thus, for either free or adiabatic expansion, the implied ratio $E_{51}/M_{\rm ej}$ is much greater than those found for most young Galactic SNRs (see, e.g., Smith 1988). We note that the only other well-documented large value for $E_{51}/M_{\rm ej}$ is for G320.4−1.2, the SNR associated with PSR B1509−58 (Gaensler et al. 1999 and references therein). This is intriguing as PSR J1119−6127 and PSR B1509−58 are very similar (see § 1, Table 1); it raises the possibility that their large magnetic fields are related to a common evolutionary scenario. For example, Gaensler et al. (1999) suggest that the progenitor of PSR B1509−58 was a massive star that later evolved into a helium star before it underwent a supernova.

4.2. *X-Ray Properties of G292.2−0.5*

4.2.1. *Spectrum*

In principle, one of the most surprising aspects of the spectrum is the lack of obvious line features commonly seen in young SNRs such as Cas A (e.g., Hughes et al. 2000), Tycho (Hwang & Gotthelf 1997), MSH 15−5-2 (e.g., Tamura et al. 1996), and Pup A (Winkler et al. 1981; Berthiaume et al. 1994). However, from the MEKAL fits, it is clear that after the line-rich spectra are folded through the GIS response, the only lines that should be visible are possibly the Fe K species around 6.7 keV. In fact, the residuals above 6 keV are smaller for the MEKAL model than for the power-law model, indicating that these lines may indeed be present.

One difficulty with either of the thermal models is the large derived temperature of $kT \approx 4$ keV. Typically, even young remnants with ages less than 1000 yr have temperatures closer to 2 keV (Koyama et al. 1996; Sakano et al. 1999). One plausible explanation for this is the use of a simple plasma model assuming solar elemental abundances. In most cases, SNR spectra with sufficiently high counting statistics (a minimum of several thousand source counts) or high energy resolution ($E/\Delta E$ of several hundred, as in the case of the Focal Plane Crystal Spectrometer on *Einstein*) require nonsolar abundances and at least one nonequilibrium ionization (NEI) model to properly describe the data (e.g., Hughes et al. 2000; Winkler et al. 1981; Hayashi et al. 1994).

While the lack of any obvious line features prevents us from attempting to fit more realistic models, we explored this possibility by adjusting the abundances of the three metals with the largest number densities relative to H, namely, Si, S, and Fe. Table 3 lists the best-fit MEKAL temperatures obtained when the abundances have been multiplied by factors of 1.5, 2.0, and 3.0. As the amount of metals is increased, the temperature monotonically drops from $3.5^{+0.4}_{-0.3}$ keV to 2.8 ± 0.2 keV. The goodness of fit (χ^2) also grows, as do the systematic residuals, indicating that abundances factors of 5 to 10 greater than solar are ruled out. However, it is quite realistic to expect that the use of an NEI model in conjunction with modestly enriched abundances would result in a goodness of fit comparable to that of the power-law or MEKAL model.

The spectral fitting we performed also allows the intriguing possibility that the emission from G292.2−0.5 is nonthermal in origin. It is well established that most young SNRs have a strong nonthermal component (see Allen, Gotthelf, & Petre 1999 for a recent review). In the most commonly accepted scenario, electrons are accelerated by the remnant's shock wave to energies of $\sim$1 TeV and emit high-energy radiation via the synchrotron mechanism (e.g., Reynolds 1998). Usually, though, thermal X-rays are also present in the SNR. One notable exception is SNR G347.3−0.5, which shows no measurable thermal emission down to very low limits (Slane et al. 1999). The photon index Γ measured for G292.2−0.5 (2.3 ± 0.1) agrees well with those in the range of values reported for different regions of G347.3−0.5 (2.2, 2.4, and 2.4). This spectrum is distinctly harder than those of SNRs that exhibit both thermal and nonthermal emission, such as Cas A ($\Gamma = 3.0 \pm 0.2$), SN 1006 (3.0 ± 0.2), Kepler (3.0 ± 0.2), Tycho (3.2 ± 0.1), and RCW 86 (3.3 ± 0.2) (Koyama et al. 1995; Allen et al. 1997, 1999).

Although the spectral similarities support the idea that G292.2−0.5 may belong to a class of nonthermal remnants typified by G347.3−0.5, Slane et al. (1999) show that the properties of G347.3−0.5 can reasonably be explained if

TABLE 3

X-Ray Temperature Dependence on Elemental Abundances

kT (keV)	Abundance Factor[a]	χ^2/dof
$3.5^{+0.4}_{-0.3}$.....	1.0	351/211
3.4 ± 0.3.....	1.5	376/211
3.1 ± 0.3.....	2.0	410/211
2.8 ± 0.2.....	3.0	479/211

[a] Here, only the most common heavy elements (Si, S, and Fe) have had their abundances, as determined by Anders & Grevesse (1989), multiplied by this factor.

the remnant is in a well-advanced Sedov evolutionary phase and has an age between 19 and 41 kyr. This is in contrast to G292.2−0.5, which is extremely young and is (possibly) just entering the Sedov phase. Ultimately, the nature of G292.2−0.5, be it a typical young thermal SNR or a more exotic manifestation of the SNR phenomenon, will only be decided with additional observations.

4.2.2. *Help from Nearby Objects*

Another important aspect of the spectrum that requires explanation is the lack of soft X-rays from the eastern side of G292.2−0.5 and the rather uniformly filled morphology at high energies (cf. Figs. 1 and 2). The absence manifests itself via absorption of emission below ∼1.5 keV (Fig. 3 [*bottom row*]). Using SIMBAD, we looked for objects in the vicinity of PSR J1119−6127 that might account for the absorption. A likely candidate is Dark Cloud DC 292.3−0.4, catalogued by Hartley et al. (1986) during a systematic search of ESO/SERC Southern J survey plates for optically identified dark clouds. Their work is an extension of the work by Lynds (1962) to declinations south of −35°. Hartley et al. (1986) approximate the shape and size of each cloud with an ellipse and use three classes to characterize the density of each cloud. (The reported dimensions do not necessarily reflect the shape of the cloud [e.g., if the cloud is elongated or curved] but do give an accurate estimate of its total area.)

DC 292.3−0.4 is described by a circle with diameter 16′. Figure 4 shows the dark cloud, represented by a hatched circle, plotted on the hardband PSPC image (for brevity, we do not show the similar GIS image). DC 292.3−0.4 appears to be located at a position capable of obscuring the eastern side of G292.2−0.5, and given that the cloud is certainly not spherical, it seems quite plausible that substructure (e.g., a finger or wisp) extending across the SNR absorbs the soft X-ray emission.

A more quantitative check is to see if the cloud can account for the difference in column densities ($N_{\rm H} \simeq 1.3 \times 10^{22}$ cm^{-2}) between the two sides of the SNR. The cloud's density (class B) roughly equals the Lynds designation of opacity class (OC) 4 or 5, which, using the calibrated relationship of Feitzinger & Stüwe (1986), $A_V = 0.70$ OC + 0.5 mag, gives an extinction $A_V = 3.3$–4.0 from DC 292.3−0.4. The corresponding column density $N_{\rm H}$ can be

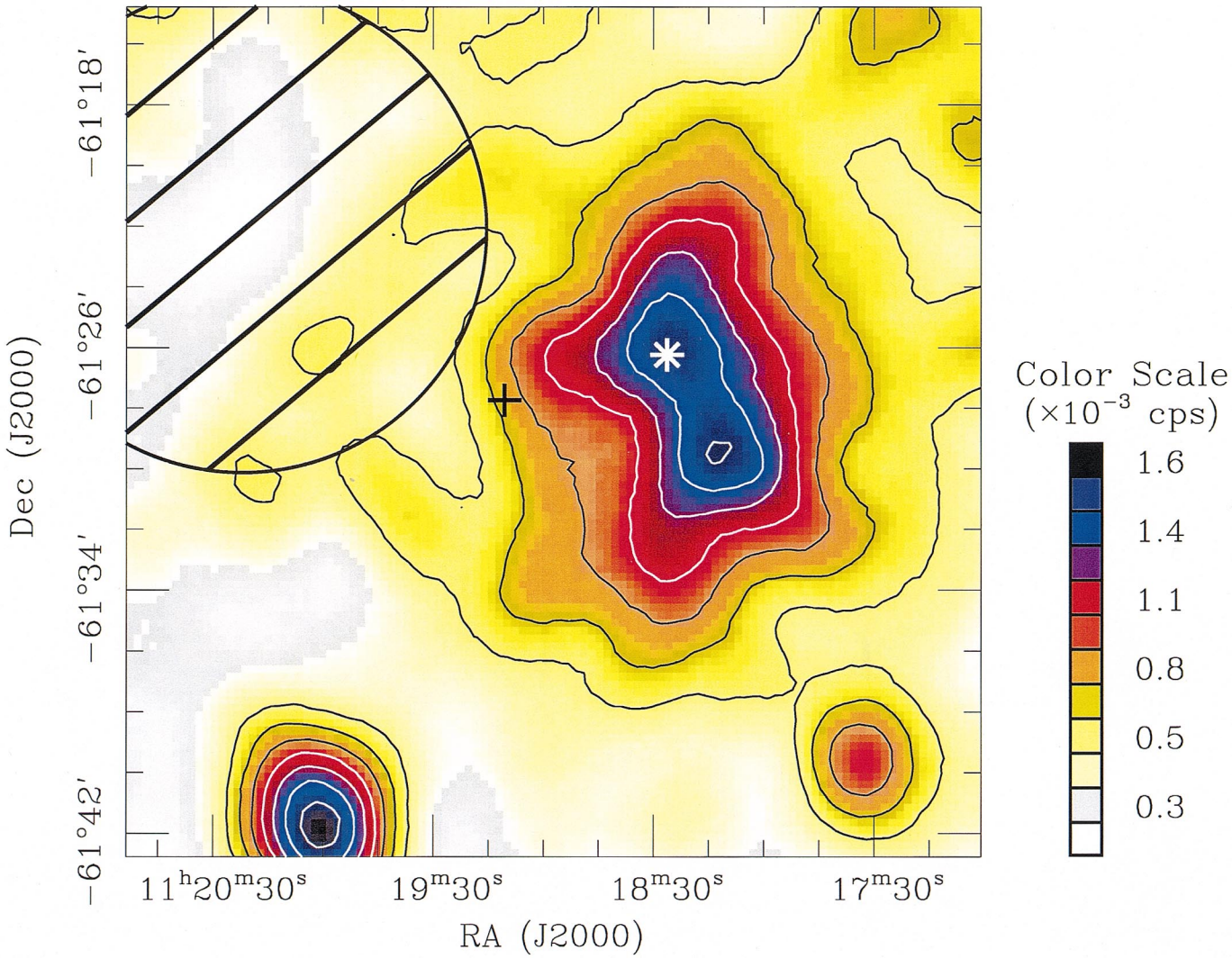

FIG. 4.—Hardband PSPC image of G292.2−0.5. The large hatched circle represents the approximate shape of dark cloud DC 292.3−0.4, which we suggest accounts for a large part of the absorption of soft X-rays from the eastern side of the SNR. The pulsar location is marked by a cross. The asterisk marks the location of HD 306313, a B9 star that is positionally coincident with enhancements in emission from the western side of the remnant in both detectors. Contours span between 35% and 95% of the maximum flux in increments of 10%.

estimated using $N_{\rm H} = 1.7 \times 10^{21}\ A_V\ {\rm cm}^{-2}\ {\rm mag}^{-1}$, derived from $\langle N({\rm H\ I})/E(B-V)\rangle = 5.2 \times 10^{21}\ {\rm cm}^{-2}\ {\rm mag}^{-1}$ (Shull & van Steenberg 1985) and $A(V)/E(B-V) = 3.1$ (Cardelli, Clayton, & Mathis 1989). Thus, we expect DC 292.3−0.4 to contribute (6–7) $\times 10^{21}$ cm^{-2} to the eastern side of G292.2−0.5, or roughly half of the additional amount of $N_{\rm H}$ present on this side of the SNR.

The presence of DC 292.3−0.4 also offers the chance to probe the distance to PSR J1119−6127. Recently, Otrupcek, Hartley, & Wang (2000) observed the 115 GHz ($J = 1$–0) transition of CO toward the center of each cloud in the Hartley et al. catalog. Two features with line-of-sight velocities of −12.6 and 1.6 km s^{-1} were detected. Unfortunately, with no way to discern which feature corresponds to the cloud, and as each feature implies two possible distance values, these CO measurements cannot provide a constraining lower limit for the pulsar's distance. The presence of two features is encouraging, however, as it suggests an additional cloud is present along the line of sight and also contributes to the absorption of soft X-rays from the eastern side of G292.2−0.5.

Figure 4 also shows the location of HD 306313 (marked with an asterisk), a B9 star with apparent magnitude 11.6. Until recently, late B stars were not thought to exhibit observable high energy emission. However, analysis of the *ROSAT* all-sky survey revealed that these stellar types can in fact be X-ray–bright (Berghöfer & Schmitt 1994; Berghöfer, Schmitt, & Cassinelli 1996). While only 10% of B9 stars emit X-rays (Berghöfer et al. 1997), this offers a possible explanation for the flux enhancements in both the PSPC and GIS images near the star. The USNO-A2.0 catalog of stars gives a blue magnitude of 12.7 and a red magnitude of 11.6 for HD 306313. The USNO calibration algorithms[15] allow us to convert to standard B and V colors, and assuming a magnitude uncertainty $\sigma = 0.25$ (Grazian et al. 2000) and correcting for the intrinsic color of a B9 star, we calculate color excesses $\langle E(B-V)\rangle$ for several stellar classes (i.e., I, III, V). Finally, adopting the absolute magnitudes measured by Jaschek & Gómez (1998) for B9 stars and the reddening law used above, we derive distances of 250 ± 80 pc (B9 V), 550 ± 165 pc (B9 III), and 6.3 ± 3.5 kpc (B9 I).

The PSPC flux (see below) from the entire western region totals $\sim 7 \times 10^{-13}$ ergs s^{-1} cm^{-2}. We estimate that the star would only need to have 1%–10% of this flux to be observable. The X-ray luminosity in the 0.1–2.4 keV band for B9 stars is in the range of log ($L_{\rm X}$) = 28.5–31.0 (Berghöfer et al. 1997). While the low flux precludes emission from a distant (i.e., more than a few kpc) supergiant, a main-sequence or giant star, with maximum unabsorbed fluxes of 1.3×10^{-12} and 2.8×10^{-13} ergs s^{-1} cm^{-2}, could easily result in the bright feature visible in the hardband PSPC and softband GIS data. Moreover, stellar emission contamination of the SNR spectrum would also explain the systematic residuals seen below 2 keV. In a detailed spectral study of A0–F6 stars, Panzera et al. (1999) show that these stars are best described by a combination of two Raymond-Smith plasma models with average temperatures of $\langle kT\rangle \sim 0.7$ keV and $\langle kT\rangle \sim 0.2$ keV. We tried adding a Raymond-Smith component to our best-fit models, but for the reasons stated in § 3.3, these attempts were unsuccessful.

We conclude with an intriguing possibility to be pursued in future observations. If HD 306313 is confirmed as an X-ray source, with sufficient data its spectral properties can be determined. By comparing its column density with that measured for the western side of G292.2−0.5, an upper or lower limit to the pulsar/remnant system can be obtained.

4.2.3. *X-Ray Luminosity*

Table 4 presents the flux measured from each side of G292.2−0.5 for each spectral model and each instrument. Luminosities have been calculated assuming a distance of 5 kpc and correcting for interstellar absorption. Formal errors on $L_{\rm X}$ are ∼5%, and regardless of the spectral model, the luminosities for a given region and instrument are within 20% of one another, guaranteeing a reliable measurement of the total luminosity from G292.2−0.5. While the *ROSAT*-measured luminosities are consistently lower than those of *ASCA*, this is easily understood given the uncertainties in calibration and differences in telescope sensitivities. The ratio between eastern and western side luminosities from *ASCA* is 2.0 ± 0.2, in excellent agreement with the 2.1 ratio of geometric areas of each region. The total 0.5–10.0 keV luminosity from G292.2−0.5 is (3–4) $\times 10^{35}$ ergs s^{-1}, after correcting for absorption and assuming a distance of 5 kpc.

4.3. *AX J1119.1−6128.5*

Figure 5 shows a close-up of the GIS hardband field surrounding PSR J1119−6127. The radio position of PSR J1119−6127 is marked by a cross, while an ellipse shows the 95% confidence uncertainty position of the unidentified infrared point source IRAS J11169−6111. The position of the IRAS source (J2000), R.A. = 11$^{\rm h}$19$^{\rm m}$07$^{\rm s}$.05, decl. = −61°27′2 6″.3, is offset 69″ from AX

[15] See http://www.nofs.navy.mil.

TABLE 4

X-Ray Flux and Luminosity for SNR G292.2−0.5

	Western Side				Eastern Side	
	ASCA		*ROSAT*		*ASCA*	
Spectral Model	$F_{0.7-7.0}$ (10^{-12})	$L_{\rm X}$ (10^{35})	$F_{0.4-2.0}$ (10^{-12})	$L_{\rm X}$ (10^{35})	$F_{0.7-8.0}$ (10^{-12})	$L_{\rm X}$ (10^{35})
Power-law	2.4	1.1 ± 0.1	0.67	$0.70^{+0.12}_{-0.08}$	3.3	$2.34^{+0.12}_{-0.08}$
Thermal bremsstrahlung	2.4	$0.94^{+0.07}_{-0.04}$	0.68	$0.58^{+0.12}_{-0.08}$	3.1	1.79 ± 0.08
MEKAL	2.4	0.94 ± 0.04	0.66	0.62 ± 0.08	3.3	1.99 ± 0.04

Note.—All fluxes, in units of (ergs s^{-1} cm^{-2}), refer to the measured absorbed flux for the given energy band, which is in keV. All luminosities, in units of (ergs s^{-1}), are for the 0.5–10.0 keV passband. They have been corrected for absorption and assume a distance of 5 kpc. All uncertainties represent the 90% confidence limits.

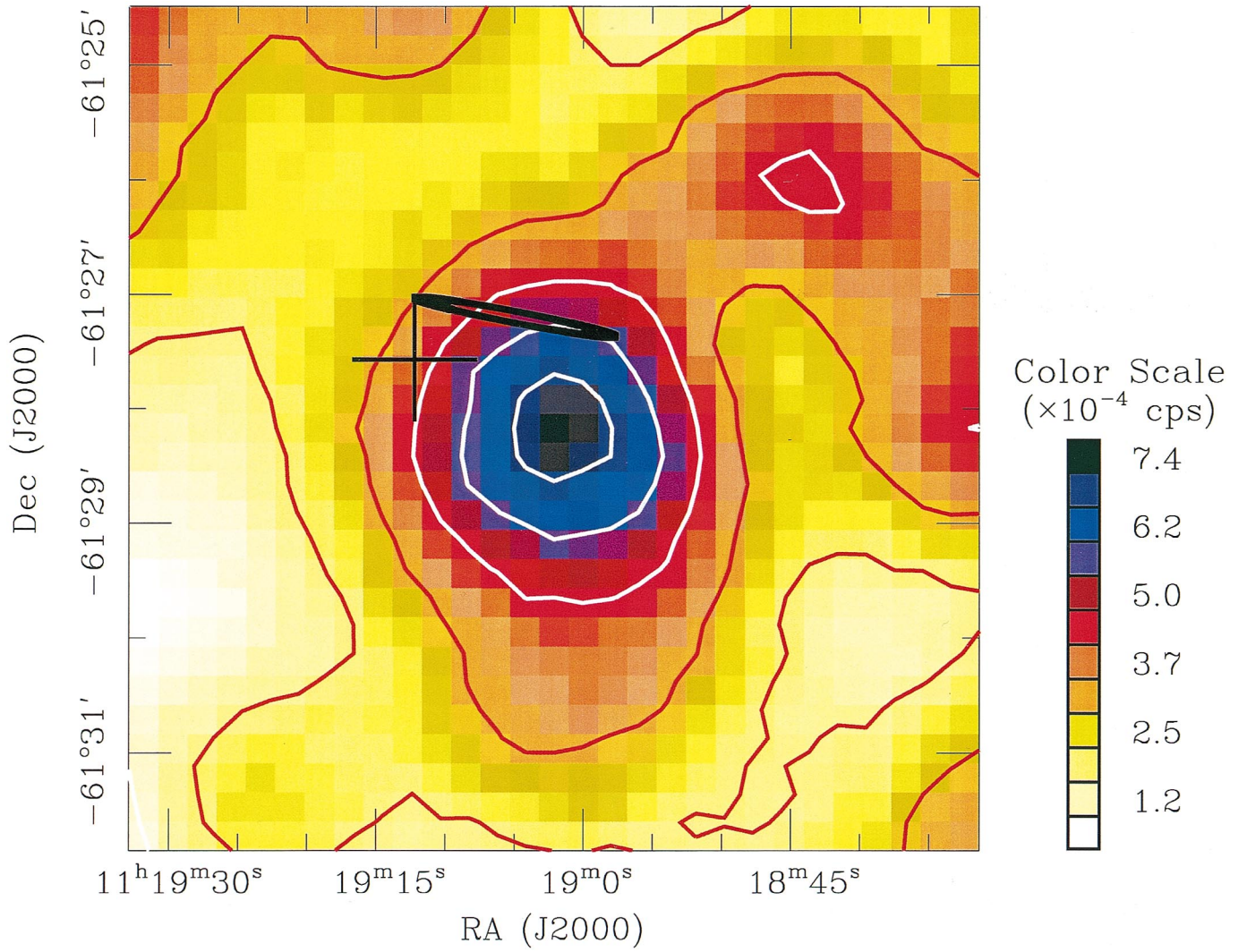

FIG. 5.—Hardband *ASCA* image of the immediate region around AX J1119.1−6128.5. A dark cross marks the location of PSR J1119−6127 (uncertainty much smaller than cross size), while a dark ellipse (semimajor axis 53″, semiminor axis 3″) marks the 95% confidence position of IRAS J11169−6111. Contours correspond to 35%–95% of the maximum flux in increments of 10%.

J1119.1−6128.5. (Recall that PSR J1119−6127 is offset 87″ from AX J1119.1−6128.5.) While the position of IRAS J11169−6111 has a large uncertainty and is slightly closer to the *ASCA* source than PSR J1119−6127, the offsets are too large to claim that AX J1119.1−6128.5 is the X-ray counterpart of the pulsar or IRAS source based solely on positional coincidence. We now consider additional evidence of relevance for both possibilities.

4.3.1. *X-Ray Luminosity*

The small number of counts from the point source precludes determining the nature of the underlying emission mechanism (e.g., thermal or nonthermal). However, by deriving the luminosity implied for various spectral models, it is possible to check the consistency of the assumption. All the luminosities reported below assume a distance of 5 kpc and have been corrected for the effects of interstellar absorption. In the case when both the photon index and normalization were allowed to vary, the implied luminosity in the 0.1–2.4 keV band is $(0.8^{+2.7}_{-0.8}) \times 10^{33}$ ergs s^{-1}, while in the 0.5–10.0 keV band it is $(2^{+25}_{-2}) \times 10^{33}$ ergs s^{-1}. The huge spread is caused by the large uncertainty in the photon index (recall $\Gamma = 0.2$–2.4; § 3.3.2). When the photon index is fixed at the usual value for young pulsars ($\Gamma = 2$), the luminosity range narrows to $(2.0 \pm 0.8) \times 10^{33}$ ergs s^{-1} for both the 0.1–2.4 and 0.5–10.0 keV bands. For the thermal bremsstrahlung model, the formal confidence limit on the temperature is $kT = 13^{+\infty}_{-11}$ keV. If we estimate the upper limit at $kT = 20$ keV, the luminosity in the 0.1–2.4 keV band is $(0.8 \pm 0.4) \times 10^{33}$ ergs s^{-1} while in the 0.5–10.0 keV band it is $(1.6^{+1.6}_{-1.2}) \times 10^{33}$ ergs s^{-1}. Thus, for either the thermal or nonthermal model, the luminosity for AX J1119.1−6128.5 in either commonly reported band (0.1–2.4 or 0.5–10.0 keV) is $L_X \sim (0.4$–$3.2) \times 10^{33}$ ergs s^{-1}.

4.3.2. *An Unresolved Synchrotron Nebula?*

If AX J1119.1−6128.5 truly has a nonthermal spectrum described by a relatively flat power law (i.e., $\Gamma \lesssim 2$), the implied X-ray luminosity is consistent with the interpretation that it is the X-ray counterpart to PSR J1119−6127. First, we consider the luminosity with a fixed photon index $\Gamma = 2$. The conversion efficiency of $\dot{E}$ into L_X is $\epsilon \equiv (L_X/\dot{E}) = (0.8 \pm 0.4) \times 10^{-3}$ for both the *ROSAT* (0.1–2.4 keV) and *Einstein* (0.2–4.0 keV) bands. These values are

close to those predicted by the L_X–$\dot{E}$ relationships of Becker & Trümper (1997 [$\epsilon = 1 \times 10^{-3}$]) and Seward & Wang (1988 [$\epsilon = 4 \times 10^{-3}$]). However, this apparent agreement must be viewed cautiously for three reasons. First, as shown by Pivovaroff et al. (2000b), both of these empirical relationships have inherent scatter of at least a factor of 4. Second, we have assumed a distance of 5 kpc for PSR J1119−6127; a reasonable range of uncertainty in this distance (§ 4.1) permits a range in L_X, and hence in ϵ, of a factor of 10. Finally, we also note that the uncertainty in ϵ greatly increases when we consider the luminosities derived from the spectral fits where both the normalization and spectral index were free parameters. More than the specific value of ϵ or whether it agrees well with a particular L_X-$\dot{E}$ relationship is the order of magnitude value: converting one part in a thousand of $\dot{E}$ into X-rays is consistent with the majority of X-ray–detected rotation-powered pulsars. If the pulsar is powering the observed high-energy emission, the lack of pulsations coupled with the pointlike nature of the source argues that AX J1119.1−6128.5 is an unresolved synchrotron nebula powered by PSR J1119−6127. This would be analogous to the X-ray emission observed by *ASCA* from PSR B1046−58 (Pivovaroff et al. 2000b), a pulsar with an $\dot{E}$ similar to that of PSR J1119−6127 but with $\tau_c = 20$ kyr.

4.3.3. *A Precursor LMXB?*

If the *ASCA* source has a hard ($kT > 2$ keV) thermal spectrum, no theoretical model or previous observational evidence supports interpreting AX J1119.1−6128.5 as the counterpart to PSR J1119−6127. Given the pointlike nature of the *ASCA* source, the emission from AX J1119.1−6128.5 could result from accretion onto a compact object. This scenario is strengthened by the nearby presence of IRAS J11169−6111, an infrared point source. Recently, two different collaborations have studied this object because of its spatial coincidence with a known S star, a red giant similar to M-class giants with prominent ZrO bands.

Chen, Gao, & Jorissen (1995) claim that IRAS J11169−6111 is actually a blend of three sources. Lloyd Evans & Little-Marenin (1999) discovered two "very red" objects at the IRAS position, although their observations resolved only a single object at the telescope. They reclassify the (possibly) composite spectrum as M3. Although isolated late-type stars can emit X-rays, their spectra are very soft ($kT < 0.5$ keV; Hünsch et al. 1998 and references therein) and cannot explain the emission from AX J1119.1−6128.5. Late-type giants, including M and S stars, in binary systems with white dwarfs can have slightly harder spectra, with kT approaching ~ 1 keV (Jorissen et al. 1996; Hünsch et al. 1998), although such a system would still not be hard enough to explain the *ASCA* source. Even if this star had unprecedented hard emission similar to AX J1119.1−6128.5, it would also need a ratio of X-ray flux to bolometric flux several orders of magnitude higher than all other known X-ray–bright M stars (Hünsch et al. 1998).

A more plausible explanation is provided by analogy with the hard X-ray emitter 2A 1704+241 (4U 1700+24). This X-ray source was first identified in the *Ariel V* 2A catalog (Cooke et al. 1978) and reconfirmed in the fourth *Uhuru* catalog (Forman et al. 1978). Using data from *Einstein* and *HEAO-1*, Garcia et al. (1983) found the spectrum well described by a highly absorbed ($N_H \sim 10^{22}$ cm^{-2}), hard ($kT = 15$ keV) thermal bremsstrahlung model and a 2.0–11.0 keV luminosity between 10^{33} and 10^{34} ergs s^{-1}. They also identified the M3 giant HD 154791 as its optical counterpart.

More recently, Gaudenzi & Polcaro (1999) performed detailed optical spectroscopy of this system and hypothesized that the observed X-ray emission is powered by accretion onto a neutron star. Moreover, they claim that this system is in the process of evolving into a normal LMXB. Dal Fiume et al. (2000) present recent *ASCA* and *BeppoSAX* observations of 4U 1700+24. In agreement with the results of Garcia et al. (1983), they find that the emission is best described with a thermal bremsstrahlung model, although with lower temperatures of $kT = 6.3$ and $kT = 3.6$ keV for *ASCA* and *BeppoSAX*, respectively. They also show that during both the *ASCA* and *BeppoSAX* observations, each of which spans 40 ks, the source experienced variability by a factor of 2. Equally intriguing, the time-averaged luminosities derived for the *ASCA* and *BeppoSAX* observations varied by nearly a factor of 3. In contrast to Gaudenzi & Polcaro (1999), Dal Fiume et al. (2000) claim that the X-ray emission is powered by accretion from the M3 giant onto a white dwarf. Whatever the nature of compact object, a similar scenario of accretion from IRAS J11169−6111 onto a neutron star or white dwarf could explain both the luminosity and spectrum of AX J1119.1−6128.5. In this case, the X-ray binary would be completely unrelated to PSR J1119−6127. We note that because of the absence of the Risetime information for our *ASCA* data mode (see § 2) and the resulting poor background subtraction (see § 3.2), we cannot rule out variability in AX J1119.1−6128.5.

5. CONCLUSIONS

We have detected X-ray emission from the direction of the young radio pulsar PSR J1119−6127 in observations with the *ASCA* and *ROSAT* satellites. X-ray emission is detected from a nearly circular region of diameter $\sim 17'$ that roughly matches the morphology of the shell-type SNR observed at radio wavelengths. We identify this as the X-ray–bright SNR G292.2−0.5. Without further observations, it is not possible to characterize the spectral properties of this SNR, with either thermal or nonthermal emission possible. The total 0.5–10.0 keV luminosity from G292.2−0.5 is (3–4) $\times 10^{35}$ ergs s^{-1}, after correcting for absorption, and assuming a distance of 5 kpc.

The radio pulsar is located near the center of the shell of radio and X-ray emission, and we have detected a hard pointlike X-ray source about 1.5 southwest of the pulsar with the *ASCA* GIS instrument. While this offset is larger than expected from the fitting procedure and *ASCA* pointing uncertainty, it is not impossibly so, and we consider the possible association of the X-ray point source AX J1119.1−6128.5 with PSR J1119−6127. No pulsations are detected from this source, with a 95% confidence upper limit of 61% for a sinusoidal profile. It is not possible to fit a unique spectral model to the point source, given limited counting statistics; however, the data are well described by a power-law model with photon index $\Gamma \approx 1$–2. For either thermal or nonthermal models, the luminosity for AX J1119.1−6128.5 in either the 0.1–2.4 or 0.5–10.0 keV bands is $L_X \sim (0.4\text{–}3.2) \times 10^{33}$ ergs s^{-1}, assuming a distance of 5 kpc. This luminosity is (0.2–1.2) $\times 10^{-3} \dot{E}$, where $\dot{E} = 2.3 \times 10^{36}$ ergs s^{-1} is the pulsar spin-down luminosity. This, of course, is the maximum luminosity being produced in

X-rays by the pulsar plus plerion combination: if AX J1119.1−6128.5 is not associated with PSR J1119−6127, L_X is smaller, i.e., $L_X/\dot{E} \lesssim 0.1\%$. For comparison, PSR B1509−58, the radio pulsar "most similar" to PSR J1119−6127 (see Table 1), has $L_X/\dot{E} = 1\%$ (Seward et al. 1984). These two young but slowly spinning pulsars therefore could have a similar efficiency for conversion of $\dot{E}$ into L_X.

However, a very recently discovered X-ray pulsar in SNR G29.7−0.3 suggests a more complex picture. PSR J1846−0258 is a rotation-powered pulsar with a period of 0.32 s, $\tau_c = 720$ yr, $B = 4.8 \times 10^{13}$ G, and $\dot{E} = 8.3 \times 10^{36}$ ergs s^{-1} (Gotthelf et al. 2000b). Given its rotational and derived parameters, PSR J1846−0258 is quite similar to PSR J1119−6127 (Table 1). Yet, for PSR J1846−0258, $L_X/\dot{E} = 25\%$, while $L_X/\dot{E} \leq 0.12\%$ for PSR J1119−6127. Although uncertain distances could moderate this discrepancy, they are unlikely to solve it. The difference could well be real, implying that the efficiency of conversion of $\dot{E}$ into L_X for young pulsars depends on more than just present spin parameters—e.g., on the evolutionary state of the pulsar–SNR system or the local ISM conditions. It is also worth noting that with the recent discoveries of PSRs J1119−6127 and J1846−0258, three of the four youngest pulsars in the Galaxy (as ranked by characteristic age) have spin periods in the range 0.15–0.4 s and very high inferred magnetic fields; only the Crab spins rapidly. This emphasizes that understanding the Crab pulsar and its nebula is not akin to understanding young pulsar–SNR systems in general, and more sensitive follow-up studies of systems such as PSR J1119−6127–SNR G292.2−0.5 are essential.

Support for this work was provided by a NASA LTSA grant (NAG 5-8063), ADP grant (NAG 5-9120), and NSF CAREER award (AST-9875897) and an NSERC Grant (RGPIN228738-00) to V. M. K. F. Camilo is supported by NASA grant NAG 5-9095. B. M. G. acknowledges the support of NASA through Hubble Fellowship grant HF-01107.01-98A awarded by the Space Telescope Science Institute, which is operated by the Association of Universities for Research in Astronomy, Inc., for NASA under contract NAS 5-26555. This research made use of the SIMBAD database, operated at CDS, Strasbourg, France, as well as the HEASARC database, maintained by NASA. We also wish to thank Mallory Roberts for his assistance with some of the figures.

REFERENCES

Allen, G., Gotthelf, E. V., & Petre, R. 1999, in "Evidence of 10–100 TeV Electrons in Supernova Remnants," in Proc. 26th Internatl. Cosmic Ray Conf., ed. D. Kieda, M. Salamon, & B. Dingus, Vol. 3, 480
Allen, G. E., et al. 1997, ApJ, 487, L97
Anders, E., & Grevesse, N. 1989, Geochim. Cosmochim. Acta, 53, 197
Becker, W., & Trümper, J. 1997, A&A, 326, 682
Berghöfer, T. W., & Schmitt, J. H. M. M. 1994, A&A, 292, L5
Berghöfer, T. W., Schmitt, J. H. M. M., & Cassinelli, J. P. 1996, A&AS, 118, 481
Berghöfer, T. W., Schmitt, J. H. M. M., Danner, R., & Cassinelli, J. P. 1997, A&A, 322, 167
Berthiaume, G. D., Burrows, D. N., Garmire, G. P., & Nousek, J. A. 1994, ApJ, 425, 132
Bevington, P. R., & Robinson, D. K. 1992, Data Reduction and Error Analysis for the Physical Sciences (2d ed.; New York: McGraw-Hill)
Brazier, K. 1994, MNRAS, 268, 709
Camilo, F. M., Kaspi, V. M., Lyne, A. G., Manchester, R. N., Bell, J. F., D'Amico, N., McKay, N. P. F., & Crawford, F. 2000, ApJ, 541, 367
Cardelli, J. A., Clayton, G. C., & Mathis, J. S. 1989, ApJ, 345, 245
Chen, P. S., Gao, H., & Jorissen, A. 1995, A&AS, 113, 51
Cooke, B. A., et al. 1978, MNRAS, 182, 489
Crawford, F. 2000, Ph.D. thesis, MIT
Crawford, F., Gaensler, B. M., Kaspi, V. M., Manchester, R. N., Camilo, F., Lyne, A. G., & Pivovaroff, M. J. 2001, ApJ, 554, 152
Dal Fiume, D., et al. 2000, in AIP Conf. Proc. 510, Proc. Fifth Compton Symp., ed. M. L. McConnell & J. M. Ryan (New York: AIP), 236
de Jager, O. C. 1994, ApJ, 436, 239
Dohm-Palmer, R. C., & Jones, T. W. 1996, ApJ, 471, 279
Fabian, A. C., Brinkmann, W., & Stewart, G. C. 1983, in IAU Symp. 101, Supernova Remnants and Their X-Ray Emission, ed. J. Danziger & P. Gorenstein (Dordrecht: Reidel), 119
Feitzinger, J. V., & Stüwe, J. A. 1986, ApJ, 305, 534
Forman, W., Jones, C., Cominsky, L., Julien, P., Murray, S., Peters, G., Tananbaum, H., & Giacconi, R. 1978, ApJS, 38, 357
Gaensler, B. M., Brazier, K. T. S., Manchester, R. N., Johnston, S., & Green, A. J. 1999, MNRAS, 305, 724
Garcia, M., et al. 1983, ApJ, 267, 291
Gaudenzi, S., & Polcaro, V. F. 1999, A&A, 347, 473
Gendreau, K. C. 1995, Ph.D. thesis, MIT
Georgelin, Y. M., & Georgelin, Y. P. 1976, A&A, 49, 57
Gotthelf, E. V., Ueda, Y., Fujimoto, R., Kii, T., & Yamaoka, K. 2000a, ApJ, 543, 417
Gotthelf, E. V., Vasisht, G., Boylan-Kolchin, M., & Torii, K. 2000b, ApJ, 542, L37
Grazian, A., Chistiani, S., D'Odorico, V., Omizzolo, A., & Pizzella, A. 2000, AJ, 119, 2540
Green, A. J., Cram, L. E., Large, M. I., & Ye, T. 1999, ApJS, 122, 207
Hartley, M., Manchester, R. N., Smith, R. M., Tritton, S. B., & Goss, W. M. 1986, A&AS, 63, 27
Hayashi, I., Koyama, K., Ozaki, M., Miyata, E., Tsumeni, H., Hughes, J. P., & Petre, R. 1994, PASJ, 46, L121
Hughes, J. P., Rakowski, C. E., Burrows, D. N., & Slane, P. O. 2000, ApJ, 528, L109
Hünsch, M., Schmitt, J. H. M. M., Schroder, K. P., & Zickgraf, F. J. 1998, A&A, 330, 225
Hwang, U., & Gotthelf, E. V. 1997, ApJ, 475, 665
Jaschek, C., & Gomez, A. E. 1998, A&A, 330, 619
Jorissen, A., Schmitt, J. H. M. M., Carquillat, J. M., Ginestet, N., & Bickert, K. F. 1996, A&A, 306, 467
Kaspi, V. M., Manchester, R. N., Siegman, B., Johnston, S., & Lyne, A. G. 1994, ApJ, 422, L83
Koyama, K., Petre, R., Gotthelf, E. V., Hwang, U., Matsura, M., Ozaki, M., & Holt, S. S. 1995, Nature, 378, 255
Koyama, K., Maeda, Y., Sonobe, T., Takeshima, T., Tanaka, Y., & Yamauchi, S. 1996, PASJ, 48, 249
Leahy, D. A., Darbro, W., Elsner, R. F., Weisskopf, M. C., Sutherland, P. G., Kahn, S., & Grindlay, J. E. 1983, ApJ, 266, 160
Lloyd Evans, T., & Little-Marenin, I. R. 1999, MNRAS, 304, 421
Lynds, B. T. 1962, ApJS, 7, 1
Otrupcek, R. E., Hartley, M., & Wang, J. S. 2000, Publ. Astron. Soc. Australia, 17, 92
Panzera, M. R., Tagliaferri, G., Pasinetti, L., & Antonello, E. 1999, A&A, 348, 161
Pivovaroff, M. J. 2000, Ph.D. thesis, MIT
Pivovaroff, M., Kaspi, V. M., & Camilo, F. 2000a, ApJ, 535, 379
Pivovaroff, M., Kaspi, V. M., & Gotthelf, E. V. 2000b, ApJ, 528, 436
Reynolds, S. P. 1998, ApJ, 493, 375
Sakano, M., Yokogawa, J., Murakami, H., Koyama, K., & Maeda, Y. 1999, in Proc Japanese-German Workshop on High Energy Astrophysics, ed. W. Becker, M. Itoh (Garching: MPI), 62
Sedov, L. I. 1959, Similarity and Dimensional Methods in Mechanics (New York: Academic)
Seward, F. D., Harnden, F. R., Jr., Szymkowiak, A., & Swank, J. 1984, ApJ, 281, 650
Seward, F. D., & Wang, Z.-R. 1988, ApJ, 332, 199
Shull, J. M., & van Steenberg, M. E. 1985, ApJ, 294, 599
Slane, P., Gaensler, B. M., Dame, T. M., Hughes, J. P., Plucinsky, P. P., & Green, A. 1999, ApJ, 525, 357
Smith, A. 1988, in IAU Colloq. 101, Supernova Remnants and the Interstellar Medium, ed. R. S. Roger & T. L. Landecker (Cambridge: Cambridge Univ. Press), 119
Tamura, K., Kawai, N., Yoshida, A., & Brinkmann, W. 1996, PASJ, 48, L33
Tanaka, Y., Inoue, H., & Holt, S. S. 1994, PASJ, 46, L37
Taylor, G. I. 1950, Proc. R. Soc. London A, 201, 159
Taylor, J. H., & Cordes, J. M. 1993, ApJ, 411, 674
Trümper, J. 1982, Adv. Space Res., 2(4), 241
Ueda, Y., et al. 1999, ApJ, 518, 656
Weiler, K. W., & Panagia, N. 1978, A&A, 70, 419
Winkler, P. F., Canizares, C. R., Clark, G. W., Markert, T. H., Kalata, K., & Schnopper, H. W. 1981, ApJ, 246, L27